Distribution of dust clouds around the central engine of NGC 1068[1]

Daigo Tomono and Hiroshi Terada

Subaru Telescope, National Astronomical Observatory of Japan
650 North A'ohoku Place, Hilo, Hawaii 96720, U.S.A.

`tomono at subaru.naoj.org`

and

Naoto Kobayashi

Institute of Astronomy, Graduate School of Science, University of Tokyo
2-21-1 Osawa, Mitaka, Tokyo 181-0015, Japan

ABSTRACT

We studied the distribution of dust clouds around the central engine of NGC 1068 based on shifted-and-added $8.8 - 12.3\ \mu$m (MIR) multi-filter images and $3.0 - 3.9\ \mu$m (L-band) spectra obtained with the Subaru Telescope. In a region of 100 pc ($1''.4$) around the central peak, we successfully constructed maps of color temperatures and emissivities of the MIR and L-band continua as well as the $9.7\ \mu$m and $3.4\ \mu$m dust features with spatial resolutions of 26 pc ($0''.37$) in the MIR and 22 pc ($0''.3$) in the L-band. Our main results are: 1) color temperature of the MIR continuum scatters around the thermal equilibrium temperature with the central engine as the heat source while that of the L-band continuum is higher and independent upon distance from the central engine; 2) the peak of the $9.7\ \mu$m silicate absorption feature is shifted to a longer wavelength at some locations; 3) the ratio of the optical depths of the dust features is different from the Galactic values and show complicated spatial distribution; and 4) there is a pie shaped warm dust cloud as an enhancement in the emissivity of the MIR continuum extending about 50 pc to the north from the central engine. We speculate that material falls into the central engine through this cloud.

Subject headings: galaxies: active — galaxies: individual (NGC 1068) — galaxies: nuclei — galaxies: Seyfert — infrared: galaxies

1. INTRODUCTION

Physics around black holes, including accretion of material and launching of jets, has been a fundamental question in astronomy for a long time (e.g. Eardley & Press 1975). It is not yet clearly known how accreting material disposes of its angular momentum while falling into a black hole, and how and where a jet is launched from around a black hole. With a jet of 100 pc scale observed (e.g. Gallimore et al. 1996), active galactic nuclei (AGNs) of Seyfert galaxies are the best targets to attack the mystery of accreting material and jets.

There are two classes of Seyfert galaxies; Seyfert 1 and Seyfert 2. They have similarities and differences in, for example, their visible spectra, which are commonly known to be explained with the unified model (Antonucci 1993). According to the unified model, an AGN has a black hole at its heart. Material falls down into the black hole through an accretion disk while emitting X-ray and UV light. Throughout this paper, we define the system of the black hole and the accretion disk as "central engine" following Galliano et al. (2003). The unified model proposes three classes of clouds around the central engine. First, narrow line regions (NLRs) spread over ~ 100 pc and emit permitted and forbidden lines with velocity widths of $\lesssim 1000$ km sec^{-1}. Second, broad line regions (BLRs) in the vicinity of the central engine emit permitted lines of ~ 10000 km sec^{-1} velocity widths. Third, an opaque compact but geometrically thick dusty torus around the central engine hides the direct view to the central engine and their BLRs from our line of sight when the central engine is viewed through the torus. The dusty torus is the key to the unified model because it is the one which distinguishes Seyfert 1 and Seyfert 2: Seyfert 2 nuclei are viewed through the dusty torus and BLRs are only seen in scattered light.

NGC 1068 is one of the nearest Seyfert 2 galaxies. Many observations have revealed various features that confirm the unified model; an accretion disk of 1 pc scale (Gallimore et al. 1997, 2001), the Seyfert 1 nucleus seen in polarized light (Antonucci & Miller 1985), and NLRs (Evans et al. 1991). However, no clear image of the dusty torus has been obtained (e.g. Bock et al. 2000; Tomono et al. 2001; Rouan et al. 2004). Only recently, Jaffe et al. (2004) found a 2.1 pc scale emission component of warm (320 K) dust surrounding a more compact hot (> 800 K) dust component with the Mid-Infrared Interferometric Instrument coupled to the Very Large Telescope Interferometer. They identified the hot component as the inner wall of the dusty torus. It is a step towards clear images of the dusty torus including its temperature structure, density distribution, and relations with structures in larger and smaller scales.

---

[1]Based on data collected at Subaru Telescope, which is operated by the National Astronomical Observatory of Japan.

On the other hand, the inner radii of the dusty tori are being measured with reverberation mapping. This method measures lag time of light curves of an AGN in the V-band and that in the K-band. In reverberation mapping, the measured lag time is interpreted as the time duration in which light from the AGN reaches the inner wall of the dusty torus. Multiplying the lag with the speed of light, the inner radius of the dusty torus R_{in} can be obtained. Minezaki et al. (2004) found a good correlation between lags and absolute magnitudes in the V-band in a number of Seyfert 1 galaxies. It implies that R_{in} is governed by luminosity of the central engine. Adopting their results, minimum R_{in} for NGC 1068 is estimated to be ~ 0.045 pc from $m_V \sim 11.5$ mag (Sandage 1973). The estimated radius is consistent with the upper limit of 1 pc measured by Jaffe et al. (2004). The method seems to be promising in unveiling the innermost structures of dusty clouds around AGNs. However, we have to note that the results do not necessarily require the dusty clouds around the AGNs to be in the shape of a torus. It is still critical to obtain direct images of dusty tori.

It is best to look for a dusty torus in the infrared (IR). First, from thermal equilibrium, it is expected that dust in a torus of 10 pc scale radiates mainly around 10 μm (Pier & Krolik 1992). Next, there are absorption/emission features of carbonaceous dust at 3.4 μm and of silicate dust at 9.7 μm. Comparison of the dust features may be used to probe the temperature structure of a dusty torus as has been suggested by Imanishi (2000). Because L-band emission is dominated by dust at ~ 1000 K, the 3.4 μm absorption feature should originate from the dust clouds in a few pc from the central engine (Pier & Krolik 1992). On the other hand, the 9.7 μm absorption feature only measures the extinction towards the outer region of the dusty torus because dust of ~ 300 K, which is the dominant source of the mid-infrared (MIR) emission, is located further out from the heating source. Therefore, the combination of MIR spectra (8 – 13 μm) and L-band spectra (2.8 – 4.2 μm) would probe the temperature distribution of dust in the line of sight through the dusty torus.

This paper reports the results from observations of NGC 1068 in the MIR and in the L-band with the Subaru Telescope, which is best suited for this study with the superb image quality in IR. Two instruments, the Mid-Infrared Test Observation System (MIRTOS) and the Infrared Camera and Spectrograph (IRCS), were used with the fine pixel scales optimized for the image quality of the telescope. The remainder of this paper is organized as follows: Sections 2 and 3 describe observations and data reduction in the MIR and in the L-band, respectively; Section 4 discusses emission mechanisms of the continua, spectral and spatial change of the dust features, and distributions of warm dust clouds; and § 5 summarizes the results. Throughout this paper, we assume the redshift of 0.0038 for NGC 1068 (Bottinelli et al. 1990). One arcsecond corresponds to 72 pc at the distance of NGC 1068, assuming the Hubble constant of $H_0 = 75$ km sec^{-1} Mpc^{-1}. Galliano et al. (2003) measured positions of the various spatial structures in the NGC 1068 nucleus observed at different wavelengths

and found that the central engine is at the IR peak. We employ their registration to compare the results in the MIR and in the L-band as well as those in the literature.

2. MIR DATA

2.1. Observations

MIR imaging observations of NGC 1068 with the "silicate filters" ($\lambda/\Delta\lambda \sim 10$) at 7.7, 8.8, 9.7, 10.4, 11.7, and 12.3 μm were made on 1999 December 31, 2000 January 9, and 2000 January 18 UT. We used the MIRTOS (Tomono 2000; Tomono et al. 2000) mounted at the Cassegrain focus of the 8.2-m Subaru Telescope. Pixel scale was $0\rlap{.}''067$, corresponding to a projected distance on the sky of 4.8 pc at the distance of NGC 1068. Sequences of 96 images of 31 msec integration were obtained. Between the sequences, the telescope was nodded typically $30'$ to the north to acquire background images. In this study, the data described in Tomono et al. (2001) were reduced again with the higher computing power available today.

2.2. Shift-and-add and registration of images

Many short-exposure images with 31 msec integration time were shifted-and-added to construct high-resolution images in each filter. First, background images, which were made with averaging the short-exposure images in the nodding pair, were subtracted from the raw images. Second, bad pixels and detector array specific features were corrected. Third, the peak position of the object in each image was measured with a precision of one tenth of a pixel with Gaussian fitting. The FWHM of the Gaussian was fixed to be the same as that of the Airy pattern to pick up the brightest speckle. Fourth, each pixel of the images was divided to 10 times 10 pixels resulting with a pixel scale of $0\rlap{.}''0067$. Fifth, each image of the smaller pixel scale was shifted by registering the peak position measured in the third step. Finally, the shifted images were averaged after some images with low peak values were removed. Table 2.2 summarizes total integration time of the short-exposure images used and the ratio of the images used to those acquired.

The flux was calibrated with the standard star α Ari (Cohen et al. 1999). Flux uncertainty was estimated at about 9% from the measurement of the other standard star α CMa (Cohen et al. 1995).

The shifted-and-added image of each filter was registered and convolved to have the same FWHM of $\sim 0\rlap{.}''37$ (26 pc) as follows. The peak position of the object for each filter was

measured by Gaussian fitting of the pixels with flux more than 75% of the peak. The images were registered assuming that the peaks for each filters are at the same location on the sky (Galliano et al. 2003). The images are then Gaussian convolved so that all the images have a similar FWHM. Figure 1 shows the spatially integrated SED within a $3''.8$ diameter aperture on the registered narrow-band images. The *ISO*-SWS spectrum in the $14'' \times 27''$ aperture (Lutz et al. 2000; Sturm et al. 2000) is also shown for comparison. The flux density measured from the MIRTOS images are consistent with the flux density of the continuum in the SWS spectrum.

2.3. Grey body fitting

We fitted the MIR spectral energy distribution (SED) with a grey body emission model including the silicate feature to estimate the temperature and amount of MIR emitting dust, as well as optical depth of the silicate absorption/emission feature. It should be noted that the extracted parameters do not represent the entire physical conditions but only characterize distributions of dust in some aspects as described below. The observed SED was fitted with a model flux

$$F_\lambda(\lambda) = \varepsilon_{cont} \left(\frac{\lambda}{10 \ \mu\text{m}} \right)^{-n} B_\lambda(T_{cont}, \lambda) \times \exp[-\tau_{9.7} \times k(\lambda)], \tag{1}$$

where $B_\lambda(T, \lambda)$ is the Planck function of temperature T and $k(\lambda)$ is the optical depth of the silicate feature obtained from the IR excess towards μ Cep (Roche & Aitken 1984) and normalized at 9.7 μm.

The μ Cep extinction curve is used in this work to compare the silicate feature with the 3.4 μm feature as has been done by Roche & Aitken (1984). The 7.7 μm image was not used because the IR excess data does not cover the short wavelength. The peak wavelength of the silicate absorption feature seen in the SEDs in Figure 1 is different from that observed towards μ Cep: the peak wavelength of the absorption is shifted from 9.7 μm to 10.4 μm especially at the central peak. Because of this, the 10.4 μm image was not used in the SED fitting. See § 4.2 for a discussion on the change of the peak wavelength.

The variables T_{cont}, ε_{cont}, and $\tau_{9.7}$ were treated as free parameters for the fitting. Color temperature T_{cont} represents the temperature of warm dust grains emitting the MIR continuum (see § 4.1.1 for a discussion). The factor ε_{cont} is a product of dust emissivity at 10 μm and beam filling factor of warm dust grains of T_{cont}. Throughout this paper, we call ε_{cont} as "emissivity". The mass of the warm dust grains per unit area can be estimated as $M_{dust} = \varepsilon_{cont}/K_{abs}$, where K_{abs} is the absorption cross section per unit mass of dust grains.
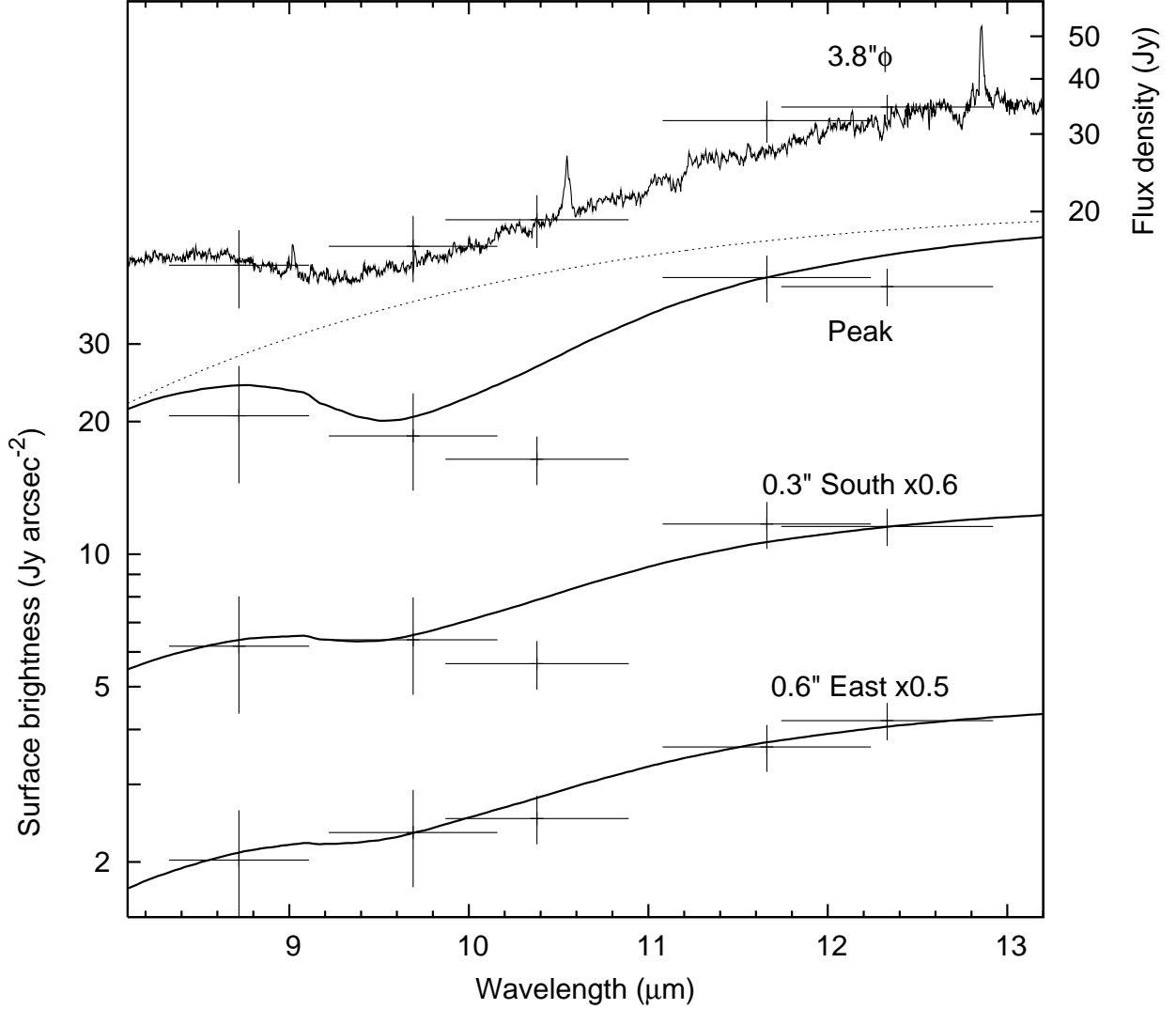
Fig. 1.— SED and results of grey body fitting in the MIR (lower data points, curves and left axis) and flux densities in a 3″.8 aperture (upper data points and right axis) compared with the spectrum measured with the *ISO*-SWS (Sturm et al. 2000, right axis). Each spatial element is measured in an area 0″.15 long (P.A. 3°) by 0″.3 wide corresponding to the *L*-band slitlet. Each data point is shown with the filter path band as a horizontal error bar and flux uncertainty of 1σ, including uncertainty in the flux conversion factor, as a vertical error bar. The thick curves display the resulting grey body models (eq. [1]) on respective spatial elements. The dotted curve shows the underlying model continuum for the peak. The 10.4 μm data are not used in fitting (see § 4.2).

The dust model (Weingartner & Draine 2001; Draine 2003) with $R_V = 5.5$ tabulates the absorption cross section at 10 μm as $K_{abs} = 0.40$ cm^2 g^{-1}. Although the dust cloud might be clumpy, clumpiness does not affect the mass estimation when $\varepsilon_{cont} < 1$ and a homogeneous temperature is assumed of warm dust that is emitting continuum. The other free parameter, $\tau_{9.7}$, is the optical depth of the silicate feature at 9.7 μm towards the warm dust that is emitting continuum. A negative optical depth in our model represents emission of the silicate feature. Although the spectral index of dust emissivity n is usually uncertain ranging from 1 to 2, we assumed $n = 1.6$ following Cameron et al. (1993). Figure 2 shows spatial distributions of the parameters fitted on each pixel. The images were successfully fitted over a region of 50 pc to the north and 40 pc to the south from the central peak: uncertainty in fitted parameters are $\Delta\tau_{9.7} < 1$, $\Delta T_{cont} < T_{cont}/2$, and $\Delta\varepsilon_{cont} < \varepsilon_{cont}/2$. Using the secondary reference star α CMa rather than α Ari, resulting T$_{cont}$ is within 1.5 K, $\tau_{9.7}$ becomes about 0.1 deeper, and ε_{cont} becomes 10% stronger. To improve the signal-to-noise ratio of the parameters in the area surrounding the central peak, the data were also fitted after being convolved to have 1.4 times wider FWHM.

Maiolino et al. (2001) pointed out that ground based measurements of the silicate absorption feature at 9.7 μm might suffer from contamination in continuum with the unidentified infrared band (UIB) emission at 7.7 μm. However, Sturm et al. (2000) detected little emission of 7.7 μm UIB towards NGC 1068 with *ISO*-SWS in the 14$''$ × 27$''$ aperture. The 3.3 μm UIB feature is not seen in the spectrum obtained towards NGC 1068 by Imanishi et al. (1997) with the 3$''$8 aperture nor in the *L*-band spectra in this work. In fact, the UIBs detected with ISOCAM (Le Floc'h et al. 2001) originate almost exclusively from the starburst regions, peaking at a distance of 1 kpc (14$''$) from the central engine. They indicated that the AGN contributes less than ∼5% to the total integrated UIB emission. Therefore, we concluded that the contamination by the UIBs to the continuum is negligible in our field of view of of ∼200 pc (2$''$7) around the central engine of NGC 1068.

High temperature areas seen 0$''$34 from the central engine on east and west sides coincide with the second and third diffraction rings (0$''$29 and 0$''$41 radius) of the Airy pattern at 8.8 μm. Between these diffraction rings, there are also diffraction rings at longer wavelengths which might affect the fitting. Nevertheless, a fitting on convolved Airy images does not reproduce a peak in fitted temperature. Therefore, we concluded that the high temperature region is not an artifact induced by the Airy rings.

Flux was also spatially integrated over the area of each *L*-band slitlet (see § 3.2) and the integrated flux is fitted with the same model as described in eq. [1]. With comparable spatial resolutions achieved for the MIR shifted-and-added images and the *L*-band seeing limited spectra, no further convolution or deconvolution was performed. Results are shown
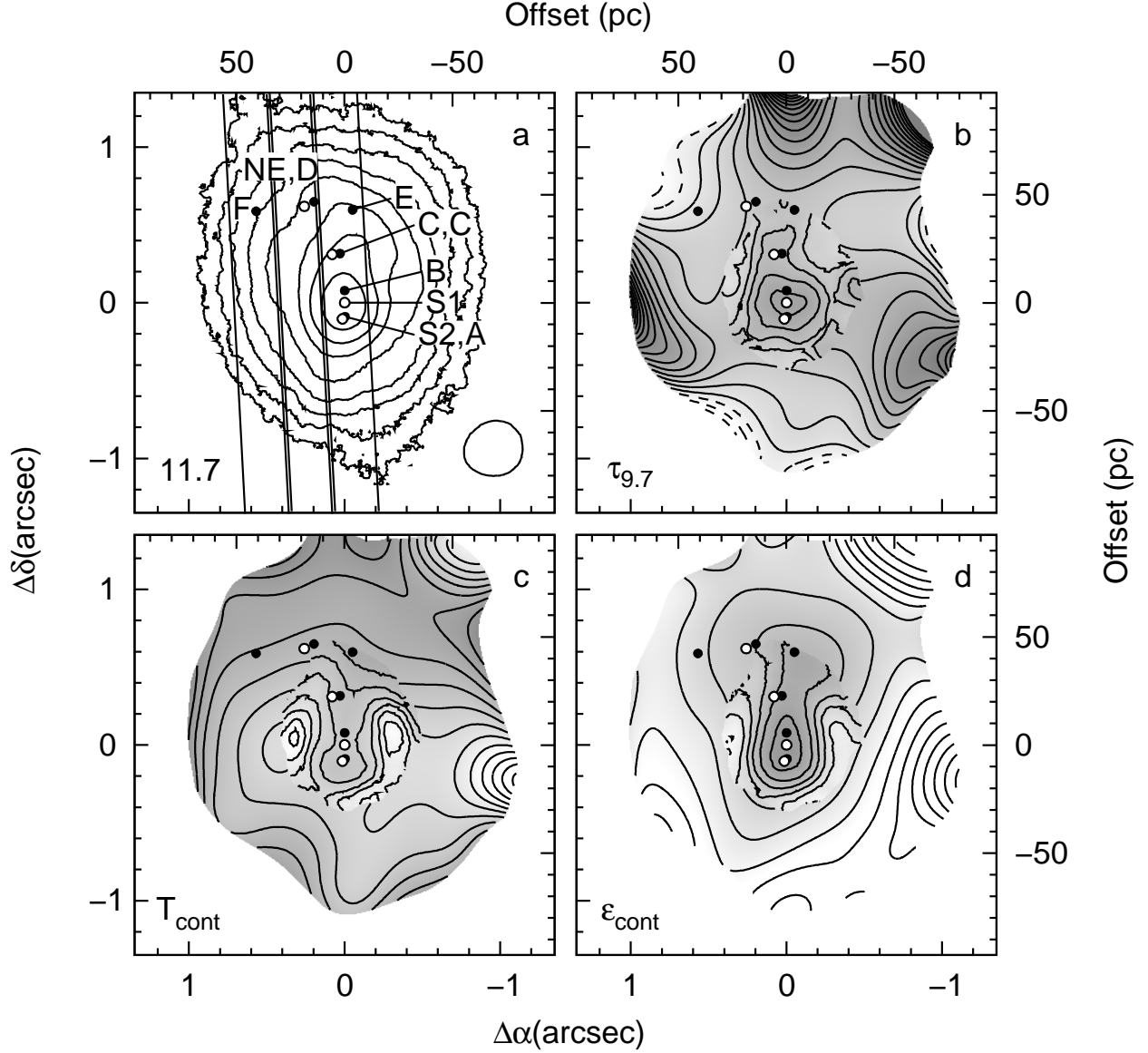
Fig. 2.— MIR image and grey body parameters (eq. [1]). The fit for the outer region is performed on images convolved with a Gaussian of FWHM same as the original PSF (the circle in panel a). Locations of the 5 GHz sources (Gallimore et al. 1996, open circles) and the [O III] clouds (Evans et al. 1991, filled circles) are indicated. (a) 11.7 μm image shown with 5 contours in dex. The straight lines show positions and widths of the three L-band slits. (b) $\tau_{9.7}$ map. Solid contours show $\tau_{9.7}$ between 0.1 and 1.5 (absorption; darker grey scale) with intervals of 0.1 while dashed contours show $\tau_{9.7}$ of 0 and -0.1 (light). (c) T_{cont}(MIR) shown with contours between 160 K (dark) and 280 K (light) with intervals of 10 K. (d) ε_{cont} shown with five contours in each dex between $10^{-1.4}$ (dark) and $10^{-3.8}$ (light).

in Figure 1.

3. *L*-BAND DATA

3.1. Observation

A seeing limited spectroscopic observation of NGC 1068 in the *L*-band was conducted on 2000 September 24 UT. We used the IRCS (Tokunaga et al. 1998; Kobayashi et al. 2000) mounted at the Cassegrain focus of the Subaru Telescope. The *L*-band grism for $2.8 - 4.2$ μm was used with the $0\rlap{.}''3$ slit, yielding the spectral resolution $\lambda/\Delta\lambda \sim 400$. The length of the slit was $18''$. Pixel scale was $0\rlap{.}''058$ pixel^{-1}. NGC 1068 was observed with the slit position angle (P.A.) of $3°$ from the north, with slit positioned at three positions to map the eastern area of the central peak: pointing offsets of $\pm 6''$ along the slit and $0\rlap{.}''28$ and $0\rlap{.}''56$ to the east were applied. Positions of the slits are illustrated in Figure 2*a*. We call the slit at the central peak as "C", and the slits in the east as "0.28E" and "0.56E" according to the offsets to the east in arcseconds. Eight exposures of 2 seconds on-source integration time were obtained for each slit position. The sky condition was photometric throughout the observation. Airmass to the target was 1.09 ± 0.01. From the size of the image along the slit, spatial resolution was estimated to be $0\rlap{.}''31$ or 22 pc in FWHM. As a telluric standard, a spectrum of BS 813 was obtained at the similar airmass (1.08). We selected a F-type star as a telluric standard because it is known that no strong stellar absorption lines are present in L-band for F-type stars. For flat fielding, spectra of dawn sky were obtained at the end of the night.

3.2. Data Reduction

The *L*-band data were reduced following the standard procedure: the 2-dimensional spectrograms were background subtracted by the dithering pairs, flat fielded, and corrected for bad pixels using IRAF[2]. Subsequently, positional shifts of the spectrograms of each slit position were measured with cross correlations and confirmed to be not more than 0.2 pixels ($0\rlap{.}''01$ or 3.2 Å) in both the spatial and dispersion directions. The spectrograms were shifted in the dispersion direction on the 2-dimensional spectrograms to cancel wavelength shifts between the slit positions. Flux of the spectrograms were then calibrated with the spectrum

---

[2]IRAF is distributed by the National Optical Astronomy Observatories, which are operated by the Association of Universities for Research in Astronomy, Inc., under cooperative agreement with the National Science Foundation.

of the standard star BS 813, which was assumed to have an effective temperature of 7244 K (Johnson & Wright 1983). Wavelengths of the spectra were calibrated using cross-correlation with a model atmospheric transmittance (Rothman et al. 1998). Then, the spectra in slitlets of 0″15 along the slit were extracted to examine spatial variations. Finally, the spectra were convolved with a Gaussian with the FWHM of 8.2Å in the dispersion direction to match the spectral resolution to that of the instrument and improve the signal-to-noise ratio.

Figure 3 shows spectra of some slitlets in the slit C. It should be noted that the slopes of the continuum at $\lambda < 3.0\ \mu$m and $\lambda > 3.9\ \mu$m are sensitive to the atmospheric conditions during the observation. In the following analysis, we did not use the data in these wavelength ranges to avoid the uncertainty of the continuum slope. The periodic feature at $3.46 - 3.56\ \mu$m in the spectrum of the central peak in Figure 3 is from the periodic telluric absorption in this wavelength range. Because the instrumental line profile changes upon spatial distribution of the illumination within the slit, the difference of the instrumental line profiles of the target and the standard star causes the residual features when the two spectra are divided each other (see the detailed discussion in Goto 2003).

3.3.   The 3.4 μm absorption feature and the L-band continuum

The absorption feature around 3.4 μm by carbonaceous dust is clearly seen in the spectra in Figure 3. Following Sandford et al. (1991), optical depth of the dust feature $\tau_{3.4}$ was measured as follows: 1) the continuum level at the absorption feature was estimated by connecting the continuum levels at rest wavelengths 3.23 and 3.64 μm with straight line and 2) $\tau_{3.4}$ was derived by averaging the optical depths at two sub peaks of the dust feature at rest wavelengths 3.38 μm (2955 cm^{-1}) and 3.42 μm (2925 cm^{-1}). The 3.48 μm (2870 cm^{-1}) sub peak was not included in the measurements because of the residual telluric feature described in § 3.2. Figure 4 shows spatial change of $\tau_{3.4}$ along with $\tau_{9.7}$ and $\tau_{10.4}$.

Color temperature T_{cont} and emissivity ε_{cont} in the L-band were estimated by fitting a grey body model

$$F_\lambda(\lambda) = \varepsilon_{cont} \left(\frac{\lambda}{10\ \mu\text{m}} \right)^{-n} B_\lambda(T_{cont}, \lambda) \qquad (2)$$

to the spectra at $3.00 - 3.23\ \mu$m and $3.64 - 3.90\ \mu$m. These wavelength ranges were chosen to avoid the 3.4 μm dust feature and the unstable continuum level at the both ends of the wavelength range due to changes of the atmospheric conditions. We assumed a dust emissivity index of $n = 1.6$ for comparison of the parameters with those in the MIR (§ 2.3). Spatial change of the color temperature in the L-band along with those in MIR are shown in Figures 5.
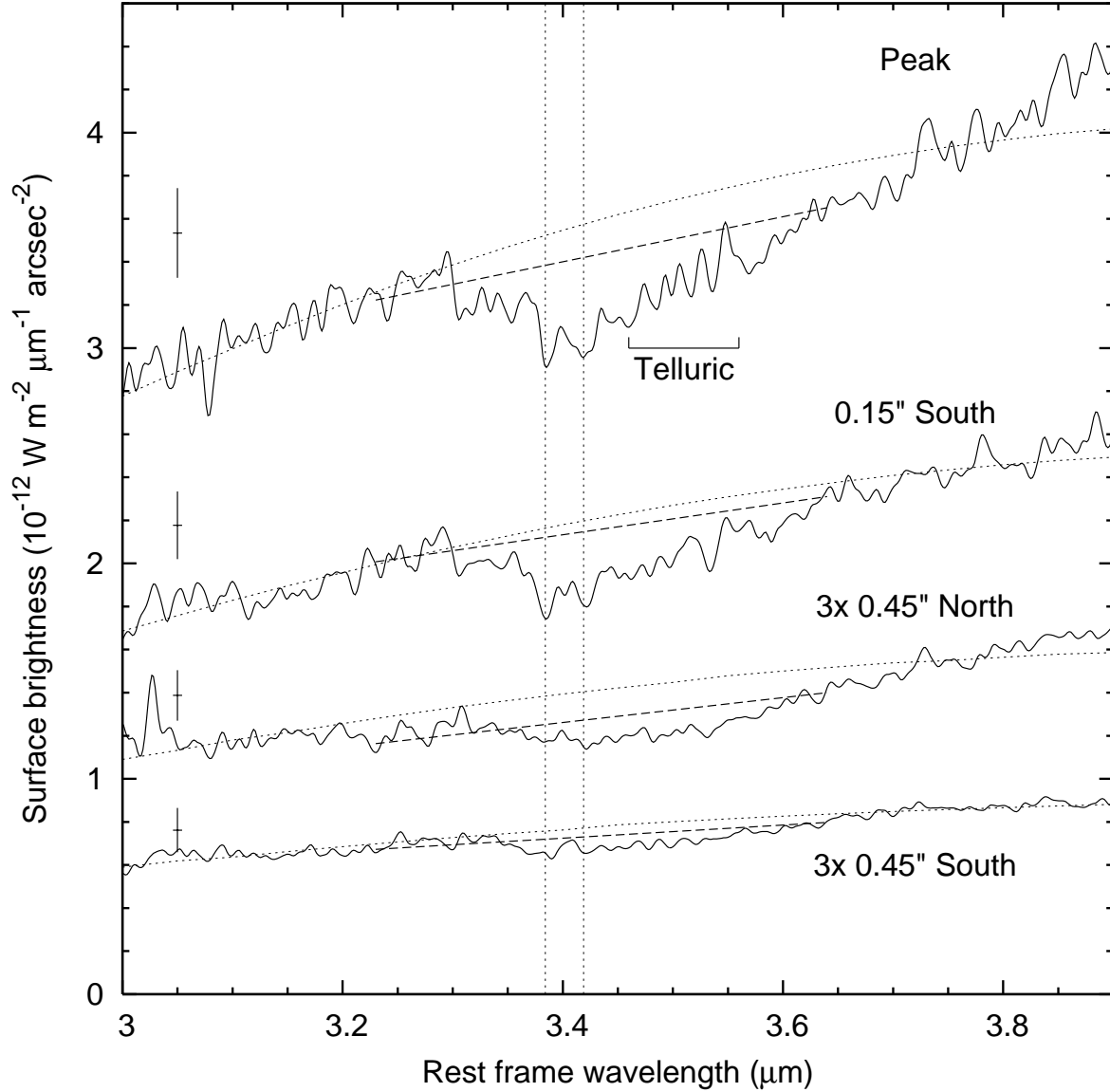
Fig. 3.— L-band spectra on slitlets of $0\rlap{.}''15$ long and $0\rlap{.}''3$ wide. Two vertical dotted lines at 3.23 μm (2955 cm^{-1}) and 3.64 μm (2925 cm^{-1}) show the location of the sub-peaks of the 3.4 μm absorption features. The dashed lines connecting continuum levels at 3.23 and 3.64 μm show continua for measuring $\tau_{3.4}$ (Sandford et al. 1991). The dotted curves show model continuum (eq. [2]) with dust emissivity index of $n = 1.6$, fitted for the data between 3.0 and 3.9 μm excluding the wavelength range of the dust feature (3.23 and 3.64 μm). The crosses in the left show typical 1σ statistical uncertainties (vertical length) of each data point and the spectral resolution (horizontal length). Periodic features between 3.46 and 3.56 μm seen in some spectra are artifacts due to telluric absorption (Goto 2003).
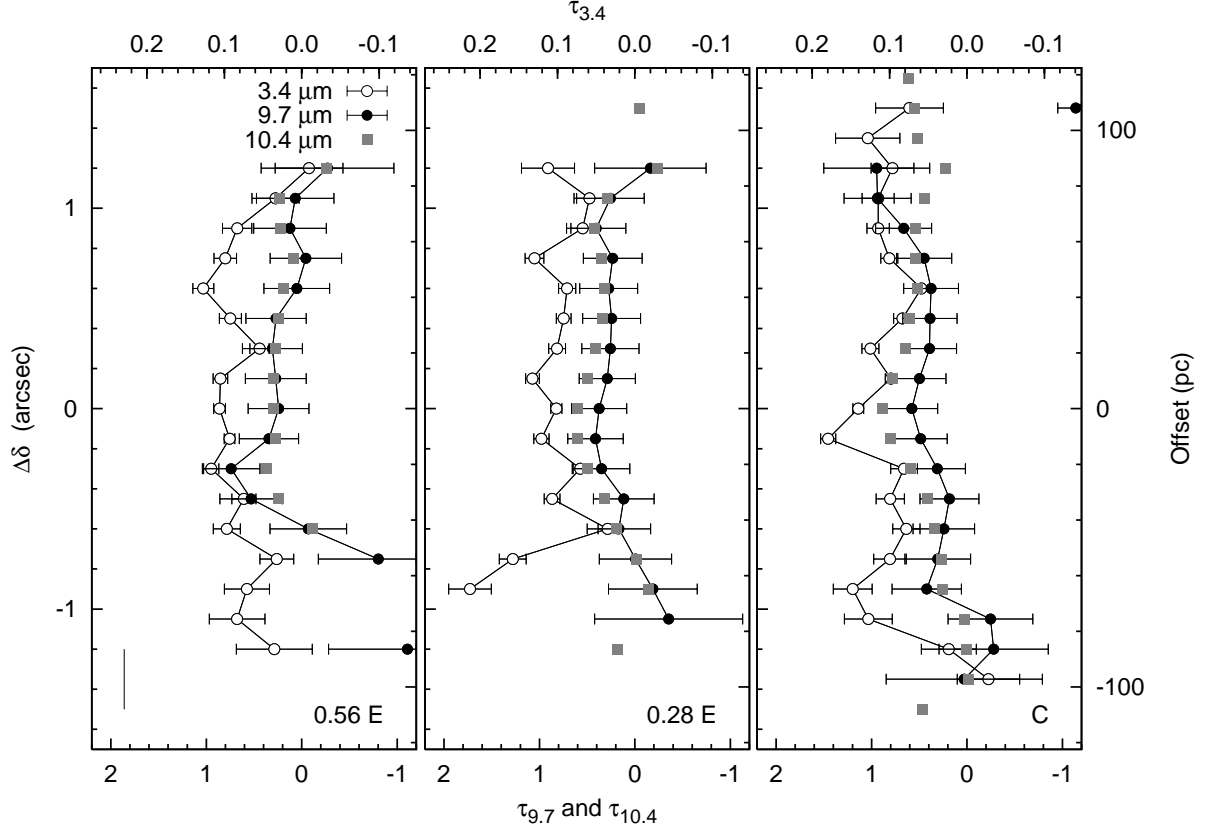
Fig. 4.— Spatial variation of optical depths of the dust features for three slit positions. Open circles, filled circles, grey filled squares show $\tau_{3.4}$, $\tau_{9.7}$, and $\tau_{10.4}$, respectively. Positive values of τ mean absorption while negative values mean emission. Error bars are the 1σ uncertainty. Error bars for $\tau_{10.4}$, which are similar to that for $\tau_{9.7}$, are not shown. The vertical line at bottom left shows the spatial resolution (FWHM) of the data.
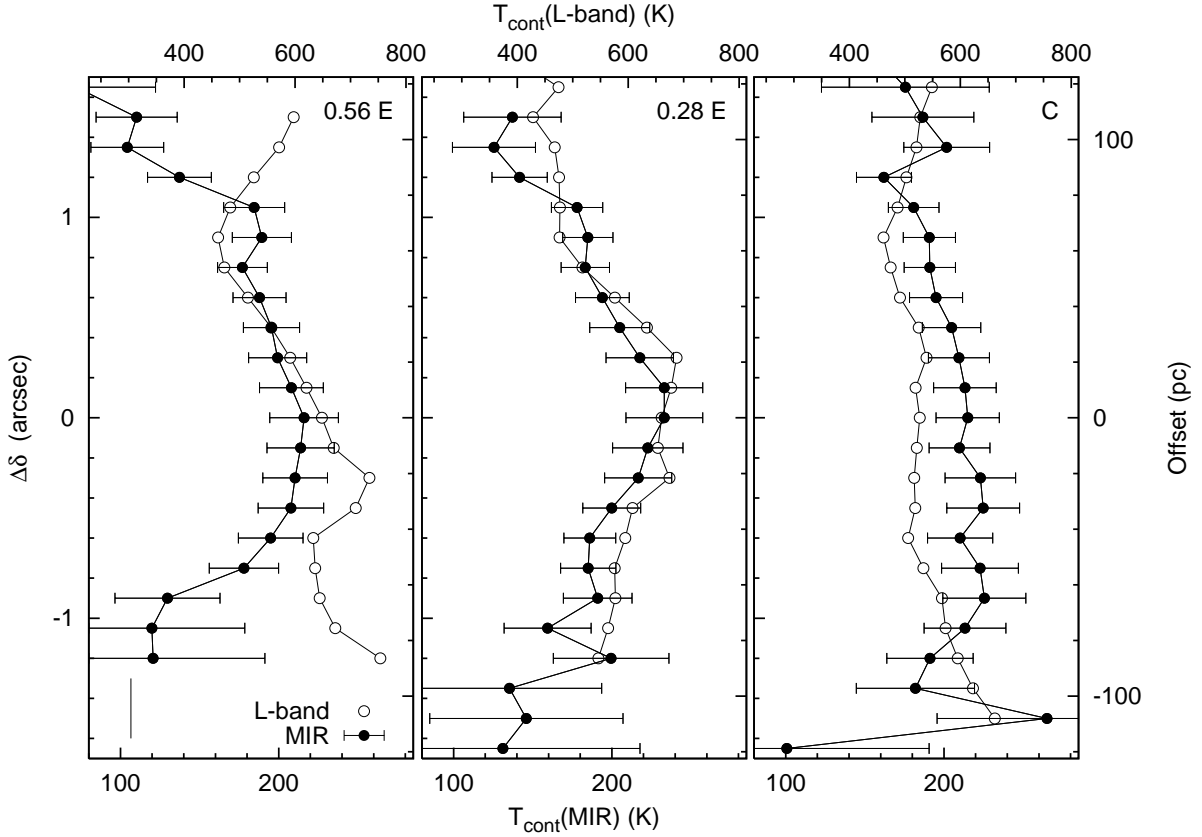
Fig. 5.— Color temperatures of the continua in the *L*-band (open circles and upper abscissa) and in the MIR (filled circles and lower abscissa) on the three slit positions. Error bars show the 1σ uncertainty of each measurement, which are less than the size of the symbols for the *L*-band measurements. The vertical line at bottom left shows the spatial resolution (FWHM) of the data.

4. RESULTS AND DISCUSSION

4.1. Emission mechanisms of MIR and L-band continua

Continua are detected both in the MIR and in the L-band over a region of 100 pc to the north and to the south from the central engine. Because Gratadour et al. (2003) detected no evidence of stellar activity in the vicinity of the central engine in their K-band spectra, stellar activity should be negligible as a source of the extended IR continua. In the following, we will show that the MIR continuum is emitted from dust in thermal equilibrium with the UV radiation from the central engine while the continuum in the L-band is emitted by Very Small Grains (VSGs).

4.1.1. MIR continuum emission

Assuming a dust emissivity index n 1.6, Cameron et al. (1993) estimated dust temperature T in thermal equilibrium with a UV radiation field as

$$R = 0.14 \left(\frac{L}{1.5 \times 10^{11} \ \mathrm{L_\odot}} \right)^{0.5} \left(\frac{T}{1500 \ \mathrm{K}} \right)^{-2.8} \mathrm{pc}, \tag{3}$$

where L is the luminosity of the UV source and R is the linear distance from the heating source. Figure 6 shows color temperature T_{cont} measured in the MIR and the estimated temperature for $L = 2.2 \times 10^{11} \ \mathrm{L_\odot}$ (Telesco & Harper 1980, at luminosity distance of 15 Mpc) as a function of the distance from the central engine. The distance is assumed to be the same as the projected distance on the sky. The vertical dotted lines in the Figure show spatial resolutions of data in the MIR and in the L-band, which are different because of different wavelengths and observation conditions. Because the light from the central engine, of which color temperature might be different from that for the extended continua, might contaminate the continua, the color temperatures measured around the central engine within the spatial resolutions are not accurate.

In Figure 6, the measured T_{cont} in the MIR scatters around the estimated equilibrium temperature. This implies that, as a whole, the MIR emitting dust is mainly heated by the central engine and is in thermal equilibrium as has been suggested by Galliano et al. (2005).

4.1.2. L-band continuum emission

We interpret that the extended L-band continuum is emitted by VSGs among the following three possibilities. First, the continuum is not dominated by the scattered light of
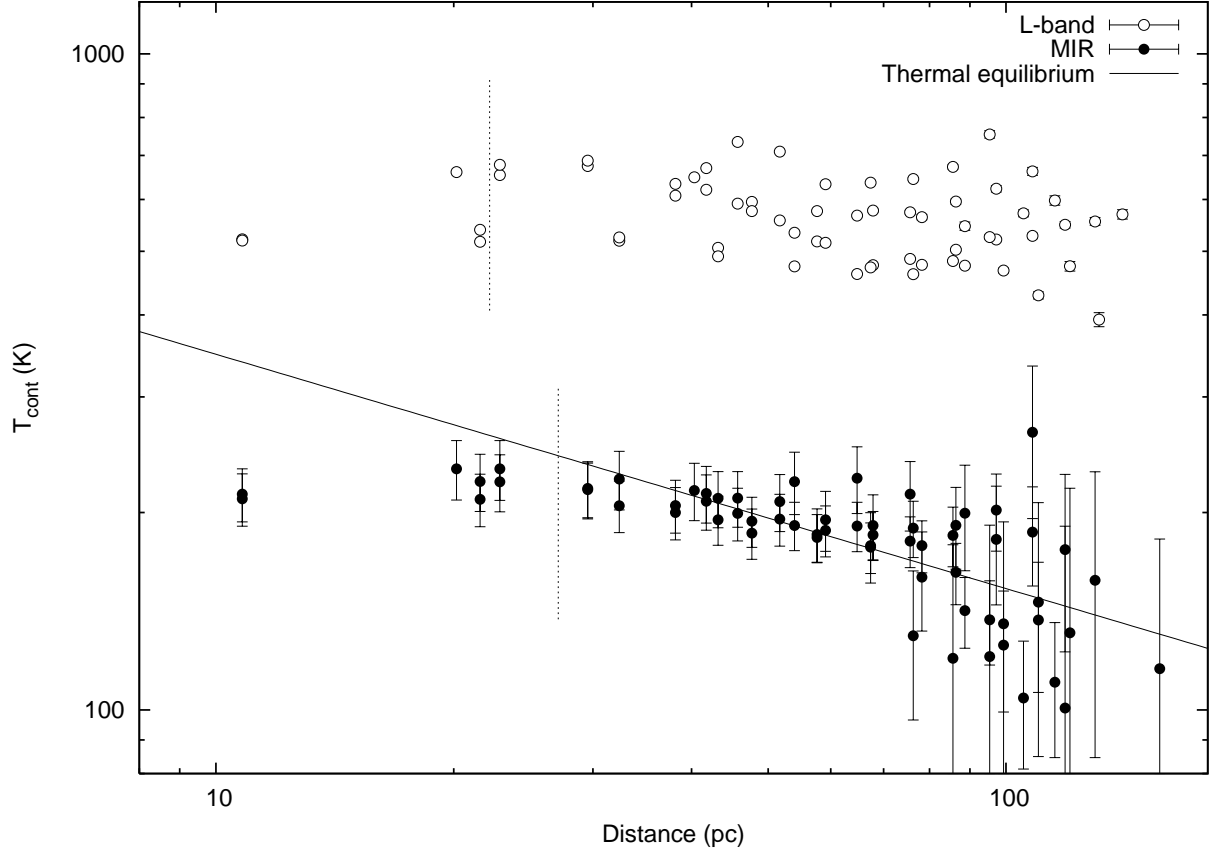
Fig. 6.— Color temperatures of continua measured on each slitlet in MIR (filled circles) and in the L-band (empty circles). Horizontal axis shows projected distance on the sky from the central engine. Error bars show the 1σ uncertainty of each measurement, almost of which are less than the size of the symbols for the L-band measurements. The solid line shows thermal equilibrium temperature of dust (eq. [3]) heated by a UV source of $L = 2.2 \times 10^{11}$ $L_{\odot}$ (Telesco & Harper 1980). The spatial resolutions of the data and contamination of light from the peak limit the color temperatures to be accurate only to the right of the vertical dotted lines (see text).

the continuum from the central engine. Packham et al. (1997) measured spatially resolved polarization degrees in the J, H, and K-bands around the central engine and found that they are not more than than 5%. Second, the L-band continuum is not emitted from dust in thermal equilibrium. As shown in Figure 6, color temperature of the L-band continuum is higher than expected for dust in thermal equilibrium. Third, color temperature in the L-band remains roughly constant as far as 100 pc from the central engine; suggesting that hot grains emitting L-band continuum exist in this area even if their column density is not as high as those emitting MIR continuum. As Rouan et al. (2004) and Gratadour et al. (2005) suggested, the uniformity of the color temperature can be explained as emission from VSGs, which emit continuum with color temperature higher than their equilibrium temperature due to thermal fluctuation upon absorption of UV photons (Sellgren 1984; Sellgren et al. 1985).

If the continuum is emitted by VSGs, the incident UV photon flux does not determine color temperature but determines brightness, or emissivity in our grey body model, of the continuum. We actually found the change of emissivity of the L-band continuum upon incident UV photon flux from our grey body fittings, suggesting that the L-band continuum is indeed emitted by VSGs. Figure 7 shows correlation between $\varepsilon_{cont}(L\text{-band})/\varepsilon_{cont}(\mathrm{MIR})$ and $T_{cont}(\mathrm{MIR})$. Thermal equilibrium temperature $T_{cont}(\mathrm{MIR})$ should correlate with the UV photon flux. On the other hand, since ε_{cont} is proportional to column density of dust grains emitting the continuum, $\varepsilon_{cont}(L\text{-band})/\varepsilon_{cont}(\mathrm{MIR})$ gives the ratio of dust grains excited to be VSGs to those in thermal equilibrium emitting continuum in the MIR. In more detail, energy F of UV photons absorbed by dust grains is balanced with the grey body emission with temperature T as follows:

$$F = \pi \int \varepsilon_{cont} \left(\frac{\lambda}{10 \ \mu\mathrm{m}} \right)^{-n} B_\lambda(T, \lambda) \ d\lambda \propto \varepsilon_{cont} T^{4+n}, \tag{4}$$

where ε_{cont} is the emissivity of the dust cloud at 10 μm. Division of two equations for the L-band and MIR continua leads to the following equation:

$$\frac{\varepsilon_{cont}(L\text{-band})}{\varepsilon_{cont}(\mathrm{MIR})} = \frac{F(L\text{-band})}{F(\mathrm{MIR})} \times \left[\frac{T_{cont}(\mathrm{MIR})}{T_{cont}(L\text{-band})} \right]^{4+n}. \tag{5}$$

The solid line in Figure 7 shows the fitting result when assuming $n = 1.6$ and adjusting the factor $T_{cont}(L\text{-band}) \times [F(\mathrm{MIR})/F(L\text{-band})]^{1/(4+n)}$ as a free parameter. Relation between the measured $\varepsilon_{cont}(L\text{-band})/\varepsilon_{cont}(\mathrm{MIR})$ and the measured $T_{cont}(\mathrm{MIR})$ in Figure 7 roughly matches with the assumption in the range of almost two orders of $\varepsilon_{cont}(L\text{-band})/\varepsilon_{cont}(\mathrm{MIR})$. The fitted factor (651 K) and the observed $T_{cont}(L\text{-band}) \sim 560$ K leads to $F(L\text{-band})/F(\mathrm{MIR}) \sim 0.43$, suggesting that VSGs absorb almost half of the UV energy that is absorbed by dust

Table 1.   Total integration time and usage rate of short-exposure images in MIR

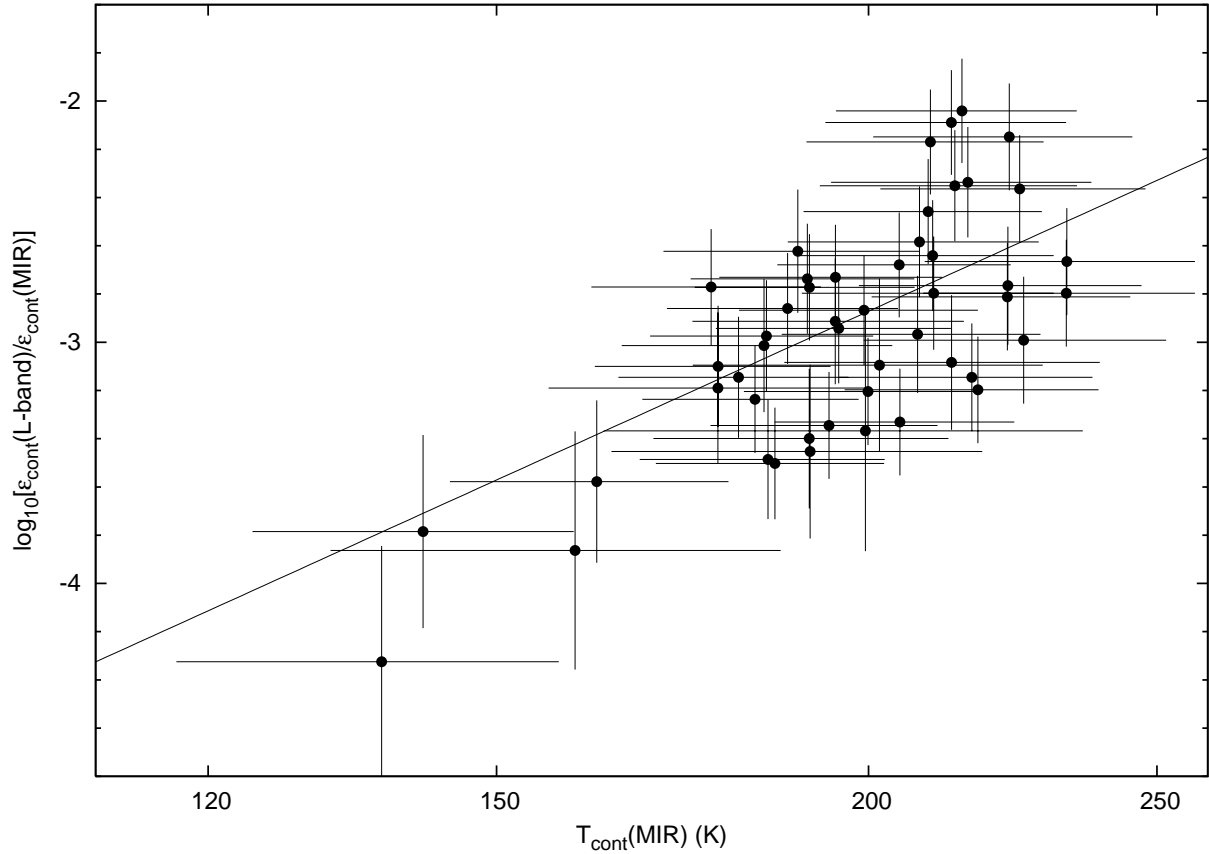| Wavelength μm	Total integration time of images used sec	Percentage of images used %
7.7	2.7	23
8.8	5.2	43
9.7	4.9	41
10.4	24.9	42
11.7	53.7	53
12.3	68.2	47

Fig. 7.— Ratio of emissivities measured in the MIR and in the L-band compared with color temperature measured in the MIR. Error bars are the 1σ uncertainty of each measurement. The solid line shows the relation $\varepsilon_{cont}(L\text{-band})/\varepsilon_{cont}(\mathrm{MIR}) = (T_{cont}(\mathrm{MIR})/651\ \mathrm{K})^{5.6}$ (eq. [5]).

grains in thermal equilibrium. The uniformity of the ratio $F(L\text{-band})/F(\text{MIR})$ suggests that dust in thermal equilibrium and VSGs are mixed well around the central engine.

4.2. Spectral profile change of the silicate absorption feature

At 10.4 μm, the silicate absorption towards the central engine is deeper than expected from the standard silicate feature. Figure 1 compares the observed SEDs with expected spectra from the IR excess towards μ Cep (Roche & Aitken 1984). There are a number of similar wavelength shift of the silicate feature in the literature. The interferometric spectrum by Jaffe et al. (2004) also shows a shift of the peak of the absorption feature towards longer wavelength. Silicate emission feature detected towards a type 1 AGN (Sturm et al. 2005) and quasars (Siebenmorgen et al. 2005) is shifted to a longer wavelength.

The spatially integrated SED in Figure 1 is consistent with the spectrum observed through the $14'' \times 20''$ aperture of the *ISO*-SWS (Sturm et al. 2000) which shows the normal spectral profile of the silicate absorption feature. This suggests that the spectral profile is normal as a whole and there is a spatial change of the profile.

To measure the optical depth of the feature without being affected by the change, we fitted the MIR SED with a gray body emission model without using the 10.4 μm image (§2.3). If the 10.4 μm image were included in the grey body fitting, the resulting $\tau_{9.7}$ would have been higher than expected from the literature (Roche et al. 1984; Tomono et al. 2001), especially near the central engine where $\tau_{9.7}$ would have to be significantly adjusted for the low flux at 10.4 μm.

Figure 8a shows spatial distribution of optical depth in the 10.4 μm filter $\tau_{10.4}$. It is measured with comparing the 10.4 μm image with the model continuum surface brightness fitted from the other images. The shape of the 10.4 μm absorption area is different from the 9.7 μm absorption area (Figure 2b). To illustrate the difference, we compared the measured $\tau_{10.4}$ with that expected from the measured $\tau_{9.7}$ and the IR excess towards μ Cep (Roche & Aitken 1984). Figure 8b shows the excess optical depth at 10.4 μm ($\Delta\tau_{10.4}$) near the central engine and to the north north east.

The change of the spectral profile might be due to change of dust properties as suggested by Siebenmorgen et al. (2005) and Sturm et al. (2005) for type 1 AGNs and quasars. The area with large $\Delta\tau_{10.4}$ in Figure 8b coincides with the pie shaped high emissivity area (§ 4.4) seen in Figure 2d. This suggests that the spectral profile change of the silicate absorption feature occurs in dense regions.
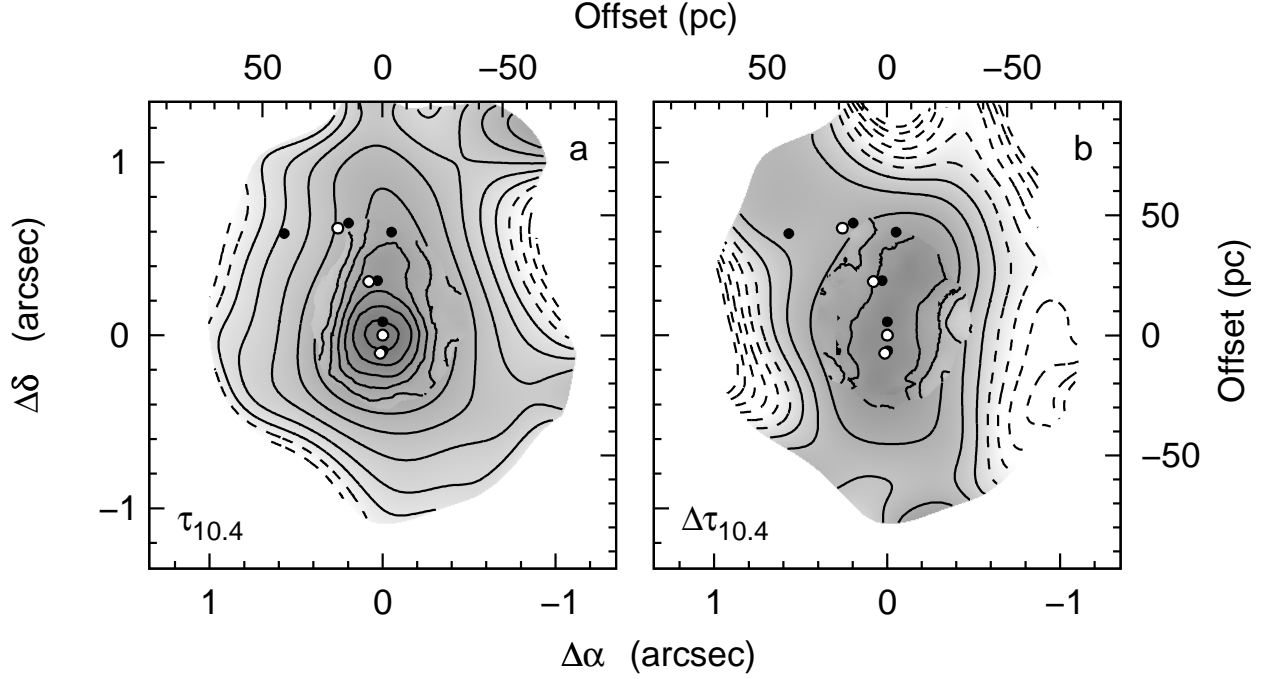
Fig. 8.— Spatial distribution of the silicate absorption feature at 10.4 μm and 9.7 μm. (a) Optical depth measured at 10.4 μm. Solid contours show $\tau_{10.4}$ between 0.1 and 0.9 (absorption; stronger with darker grey scale) with intervals of 0.1 while dashed contours show $\tau_{10.4}$ between 0 and -0.3 (emission; light). (b) Excess optical depth at 10.4 μm ($\Delta\tau_{10.4}$; see text) for the μ Cep extinction curve. Solid contours show $\Delta\tau_{10.4}$ between 0.05 and 0.35 (larger $\tau_{10.4}$; darker grey scale) with intervals of 0.1 while dashed contours show $\Delta\tau_{10.4}$ below -0.05 with intervals of 0.1. Locations of the 5 GHz sources (Gallimore et al. 1996, open circles) and the [O III] clouds (Evans et al. 1991, filled circles) are indicated.

4.3. Spatial variation of 9.7 μm and 3.4 μm absorption features

It is known that optical depth of the absorption feature of silicate dust and that of carbonaceous dust are proportional towards Galactic sources. Roche & Aitken (1984) showed that $A_V/\tau_{9.7} = 18.5$ towards Wolf-Rayet stars and B supergiants in our Galaxy. Pendleton et al. (1994) measured optical depths of the carbonaceous dust and concluded that $A_V/\tau_{3.4}$ is ~ 150 for sources in the Galactic center or ~ 250 for sources in the local interstellar matter (ISM). From these results, ratio of the optical depths of the absorption features $\tau_{9.7}/\tau_{3.4}$ is ~ 8.1 for the sources in the Galactic center or ~ 13.5 for the local ISM. Towards AGNs, $\tau_{9.7}/\tau_{3.4}$ is expected to be smaller because of temperature gradient in the dusty torus in the line of sight (Imanishi 2000). In fact, they measured $\tau_{3.4}$ towards NGC 1068 in the 3.''8 aperture, compared it with $\tau_{9.7}$ measured in the 4.''7 aperture by Roche et al. (1984), and yielded $\tau_{9.7}/\tau_{3.4} = 4.3$. With the data with higher spatial resolution, spatial variation of the ratio might show a trace of the dusty torus.

Our results show significant spatial variation of the ratio $\tau_{\mathrm{silicate}}/\tau_{3.4}$ (Figure 9), with a complexity not expected to be produced by a dusty torus. As shown in Figure 1, the 9.7 μm silicate feature is shifted towards longer wavelengths at some locations: optical depth of the feature is deeper at 10.4 μm than at 9.7 μm (§ 4.2). To minimize influence from the wavelength shift, we defined τ_{silicate} as either $\tau_{9.7}$ or $\tau_{10.4}$ whichever has the higher absolute value. At the central peak, the ratio from our observation is between that measured by Imanishi (2000) and the Galactic values. In the slit C, the ratio increases from the central peak towards the north and approaches the Galactic values. In the eastern slits, the ratio is flatter and closer to that measured by Imanishi (2000). In the south, the ratio is smaller. Figure 4 shows that the silicate feature is observed as emission in the south.

The emission of the silicate feature in the south of the central peak implies a temperature gradient in the line of sight: e.g., an optically thin layer of warm dust is present in front of cooler continuum source. On the other hand, in the north, the change of the ratio $\tau_{\mathrm{silicate}}/\tau_{3.4}$ may be explained either with a temperature gradient in the line of sight: warmer dust clouds are located behind cooler dust clouds, or with differences in dust composition. Spatially resolved MIR spectra are needed to disentangle the possibilities.

4.4. Pie shaped warm dust cloud

With the spatial resolution of 26 pc on the sky, the plausible dusty torus is not detected. Instead, we found a pie shaped area of high MIR emissivity in the north up to about 50 pc from the central engine (Figure 2d). The pie shaped area is in the west of the radio jet.
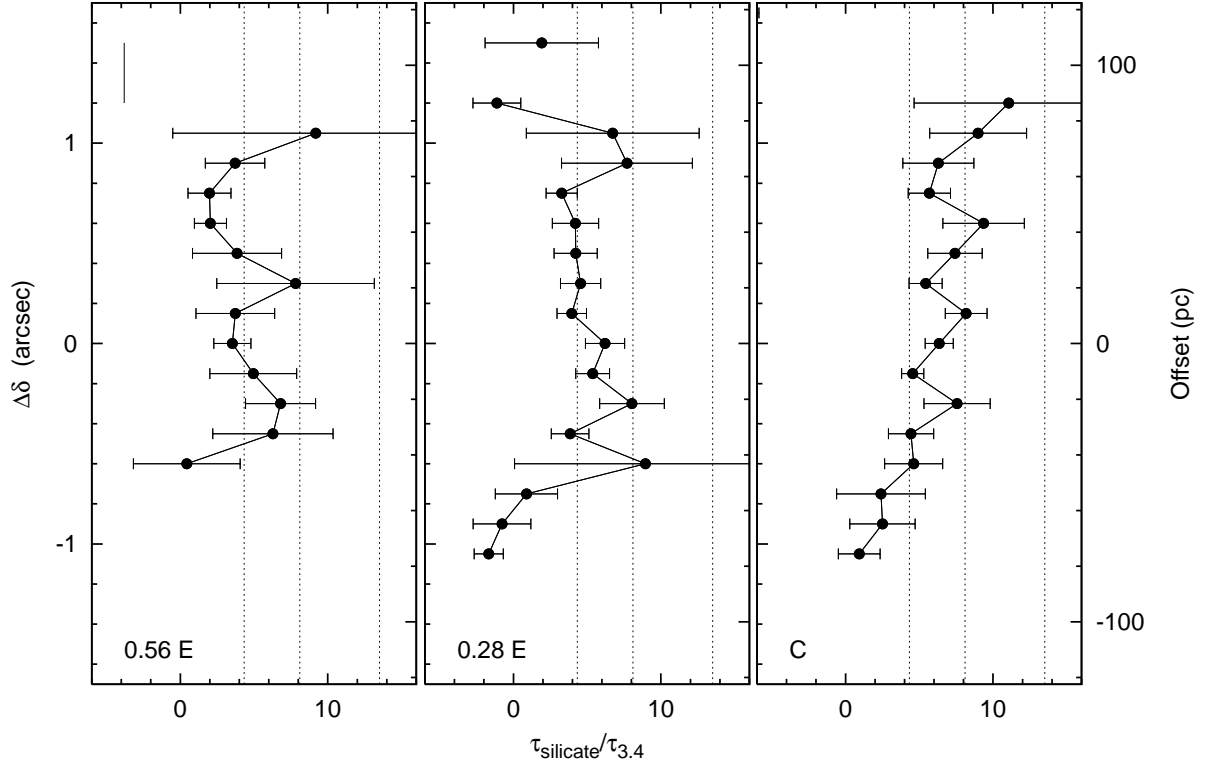
Fig. 9.— Ratio of optical depths of the dust features. The numerator τ_{silicate} is either $\tau_{9.7}$ or $\tau_{10.4}$, whichever had the higher absolute value. The vertical dotted lines from left to right show the ratios measured on the $3''\!.8 \times 3''\!.8$ aperture (Imanishi 2000), on Galactic center sources, and on local ISM (Pendleton et al. 1994), respectively. Error bars are the 1σ uncertainty of each measurement. The vertical line at top left shows the spatial resolution (FWHM) of the data.

There is no other hint of a channel supplying material to the central engine in the IR images in the literature and in this study. Therefore, we speculate that the area might be a channel that supplies material to the central engine.

The lifetime of this cloud can be estimated assuming that material falls down into the central engine through the cloud. The dust mass of the cloud is estimated at around 4.6×10^5 M$_\odot$ integrating $\varepsilon_{cont}(\text{MIR})$ over the cloud where $\varepsilon_{cont}(\text{MIR}) \geq 10^{-1.6}$ and dividing with K_{abs} (§ 2.3). Assuming the dust-to-gas ratio of 100 (Contini & Contini 2003), total mass of the cloud is $\sim 4.6 \times 10^7$ M$_\odot$. Mass accretion rate to the central engine is estimated at 0.05 M$_\odot$ year^{-1} from total luminosity $L = 2.2 \times 10^{11}$ L$_\odot$ (Telesco & Harper 1980, at luminosity distance of 15 Mpc) and a typical value of mass-to-luminosity conversion efficiency of a black hole $L \sim 0.3c^2 dM/dt$ (Eardley & Press 1975). The estimated total mass and accretion rate yields a lifetime of the cloud to be on the order of 10^9 years.

5. CONCLUSION

We observed an area of $2\rlap{.}''8$ (200 pc) around the central peak of NGC 1068 in the MIR (8.8 – 12.3 μm) and in the L-band (3.0 – 3.9 μm). The shifted-and-added MIR images have a spatial resolution of $0\rlap{.}''37$ or a projected distance of 26 pc while the L-band spectra are taken with a seeing limited spatial resolution of $0\rlap{.}''3$ or 22 pc. From these data, we derived grey body parameters: color temperatures of the continua and emissivities, which are proportional to column densities of dust emitting the continua, at each spatial element. Moreover, optical depths of spectral features of silicate around 9.7 μm and carbonaceous dust around 3.4 μm were also derived (§§ 2.3, 3.3).

The extended continua over 100 pc to the north and to the south of the central source are detected both in the MIR and in the L-band. We found that the MIR continuum is mainly emitted from dust in thermal equilibrium with radiation from the central engine while the L-band continuum is emitted by VSGs (§ 4.1). The observed SED in the MIR suggests that the peak wavelength of the 9.7 μm silicate absorption feature is shifted to a longer wavelength at some locations (§ 4.2). The ratio of the optical depths of the silicate and carbonaceous dust features show complicated spatial distribution (§ 4.3). There is a pie shaped area of enhanced MIR emissivity extending about 50 pc to the north from the central engine. The morphology of the cloud leads us to speculate that the area is a channel that feeds material into the central engine (§ 4.4).

REFERENCES

Antonucci, R. 1993, ARA&A, 31, 473

Antonucci, R. R. J., & Miller, J. S. 1985, ApJ, 297, 621

Bock, J. J., Neugebauer, G., Matthews, K., Soifer, B. T., Becklin, E. E., Ressler, M., Marsh, K., Werner, M. W., Egami, E., & Blandford, R. 2000, AJ, 120, 2904

Bottinelli, L., Gouguenheim, L., Fouque, P., & Paturel, G. 1990, A&AS, 82, 391

Cameron, M., Storey, J. W. V., Rotaciuc, V., Genzel, R., Verstraete, L., Drapatz, S., Siebenmorgen, R., & Lee, T. J. 1993, ApJ, 419, 136

Cohen, M., Walker, R. G., Carter, B., Hammersley, P., Kidger, M., & Noguchi, K. 1999, AJ, 117, 1864

Cohen, M., Witteborn, F. C., Walker, R. G., Bregman, J. D., & Wooden, D. H. 1995, AJ, 110, 275

Contini, M., & Contini, T. 2003, MNRAS, 342, 299

Draine, B. T. 2003, ARA&A, 41, 241

Eardley, D. M., & Press, W. H. 1975, ARA&A, 13, 381

Evans, I. N., Ford, H. C., Kinney, A. L., Antonucci, R. R. J., Armus, L., & Caganoff, S. 1991, ApJ, 369, L27

Galliano, E., Alloin, D., Granato, G. L., & Villar-Martín, M. 2003, A&A, 412, 615

Galliano, E., Pantin, E., Alloin, D., & Lagage, P. O. 2005, MNRAS, 363, L1

Gallimore, J. F., Baum, S. A., & O'Dea, C. P. 1996, ApJ, 464, 198

—. 1997, Nature, 388, 852

Gallimore, J. F., Henkel, C., Baum, S. A., Glass, I. S., Claussen, M. J., Prieto, M. A., & Von Kap-herr, A. 2001, ApJ, 556, 694

Goto, M. 2003, in Proceedings of the ESO Workshop on Science with Adaptive Optics held in Garching, Germany, 16-19 September 2003, ed. W. Brandner & M. Kasper, ESO Astrophysics Symposia, ESO (Springer-Verlag), in press

Gratadour, D., Clénet, Y., Rouan, D., Lai, O., & Forveille, T. 2003, A&A, 411, 335

Gratadour, D., Rouan, D., Boccaletti, A., Riaud, P., & Clénet, Y. 2005, A&A, 429, 433

Imanishi, M. 2000, MNRAS, 319, 331

Imanishi, M., Terada, H., Sugiyama, K., Motohara, K., Goto, M., & Maihara, T. 1997, PASJ, 49, 69

Jaffe, W., Meisenheimer, K., Röttgering, H. J. A., Leinert, C., Richichi, A., Chesneau, O., Fraix-Burnet, D., Glazenborg-Kluttig, A., Granato, G.-L., Graser, U., Heijligers, B., Köhler, R., Malbet, F., Miley, G. K., Paresce, F., Pel, J.-W., Perrin, G., Przygodda, F., Schoeller, M., Sol, H., Waters, L. B. F. M., Weigelt, G., Woillez, J., & de Zeeuw, P. T. 2004, Nature, 429, 47

Johnson, H. M., & Wright, C. D. 1983, ApJS, 53, 643

Kobayashi, N., Tokunaga, A. T., Terada, H., Goto, M., Weber, M., Potter, R., Onaka, P. M., Ching, G. K., Young, T. T., Fletcher, K., Neil, D., Robertson, L., Cook, D., Imanishi, M., & Warren, D. W. 2000, in Proc. SPIE Vol. 4008, p. 1056–1066, Optical and IR Telescope Instrumentation and Detectors, Masanori Iye; Alan F. Moorwood; Eds., Vol. 4008, 1056–1066

Le Floc'h, E., Mirabel, I. F., Laurent, O., Charmandaris, V., Gallais, P., Sauvage, M., Vigroux, L., & Cesarsky, C. 2001, A&A, 367, 487

Lutz, D., Sturm, E., Genzel, R., Moorwood, A. F. M., Alexander, T., Netzer, H., & Sternberg, A. 2000, ApJ, 536, 697

Maiolino, R., Marconi, A., Salvati, M., Risaliti, G., Severgnini, P., Oliva, E., La Franca, F., & Vanzi, L. 2001, A&A, 365, 28

Minezaki, T., Yoshii, Y., Kobayashi, Y., Enya, K., Suganuma, M., Tomita, H., Aoki, T., & Peterson, B. A. 2004, ApJ, 600, L35

Packham, C., Young, S., Hough, J. H., Axon, D. J., & Bailey, J. A. 1997, MNRAS, 288, 375

Pendleton, Y. J., Sandford, S. A., Allamandola, L. J., Tielens, A. G. G. M., & Sellgren, K. 1994, ApJ, 437, 683

Pier, E. A., & Krolik, J. H. 1992, ApJ, 401, 99

Roche, P. F., & Aitken, D. K. 1984, MNRAS, 208, 481

Roche, P. F., Whitmore, B., Aitken, D. K., & Phillips, M. M. 1984, MNRAS, 207, 35

Rothman, L. S., Rinsland, C. P., Goldman, A., Massie, S. T., Edwards, D. P., Flaud, J.-M., Perrin, A., Camy-Peyret, C., Dana, V., Mandin, J.-Y., Schroeder, J., McCann, A., Gamache, R. R., Wattson, R. B., Yoshino, K., Chance, K. V., Jucks, K. W., Brown, L. R., Nemtchinov, V., & Varanasi, P. 1998, J. Quant. Spec. Radiat. Transf., 60, 665

Rouan, D., Lacombe, F., Gendron, E., Gratadour, D., Clénet, Y., Lagrange, A.-M., Mouillet, D., Boisson, C., Rousset, G., Fusco, T., Mugnier, L., Séchaud, M., Thatte, N., Genzel, R., Gigan, P., Arsenault, R., & Kern, P. 2004, A&A, 417, L1

Sandage, A. 1973, ApJ, 183, 711

Sandford, S. A., Allamandola, L. J., Tielens, A. G. G. M., Sellgren, K., Tapia, M., & Pendleton, Y. 1991, ApJ, 371, 607

Sellgren, K. 1984, ApJ, 277, 623

Sellgren, K., Allamandola, L. J., Bregman, J. D., Werner, M. W., & Wooden, D. H. 1985, ApJ, 299, 416

Siebenmorgen, R., Haas, M., Krügel, E., & Schulz, B. 2005, A&A, 436, L5

Sturm, E., Lutz, D., Tran, D., Feuchtgruber, H., Genzel, R., Kunze, D., Moorwood, A. F. M., & Thornley, M. D. 2000, A&A, 358, 481

Sturm, E., Schweitzer, M., Lutz, D., Contursi, A., Genzel, R., Lehnert, M. D., Tacconi, L. J., Veilleux, S., Rupke, D. S., Kim, D.-C., Sternberg, A., Maoz, D., Lord, S., Mazzarella, J., & Sanders, D. B. 2005, ApJ, 629, L21

Telesco, C. M., & Harper, D. A. 1980, ApJ, 235, 392

Tokunaga, A. T., Kobayashi, N., Bell, J., Ching, G. K., Hodapp, K., Hora, J. L., Neill, D., Onaka, P. M., Rayner, J. T., Robertson, L., Warren, D. W., Weber, M., & Young, T. T. 1998, in Proc. SPIE Vol. 3354, p. 512-524, Infrared Astronomical Instrumentation, Albert M. Fowler; Ed., 512–524

Tomono, D. 2000, PhD thesis, Univ. Tokyo

Tomono, D., Doi, Y., & Nishimura, T. 2000, in Proc. SPIE Vol. 4008, p. 853-860, Optical and IR Telescope Instrumentation and Detectors, Masanori Iye; Alan F. Moorwood; Eds., 853–860

Tomono, D., Doi, Y., Usuda, T., & Nishimura, T. 2001, ApJ, 557, 637

Weingartner, J. C., & Draine, B. T. 2001, ApJ, 548, 296